# High Torque Density Low Voltage Traction Drives with Preformed Coils: Evaluation of Operating Limitations

Florian Pauli
Institute of Electrical Machines (IEM)
*RWTH Aachen University*
Aachen, Germany
florian.pauli@iem.rwth-aachen.de

Benedikt Groschup
Institute of Electrical Machines (IEM)
*RWTH Aachen University*
Aachen, Germany

Michael Schröder
Institute of Electrical Machines (IEM)
*RWTH Aachen University*
Aachen, Germany

Kay Hameyer
Institute of Electrical Machines (IEM)
*RWTH Aachen University*
Aachen, Germany

2020 10th International Electric Drives Production Conference (EDPC) | 978-1-7281-8458-6/20/$31.00 ©2020 IEEE | DOI: 10.1109/EDPC51184.2020.9388214

***Abstract*—The geometry of preformed coils with a varying conductor width allows a high copper fill factor in parallel teeth stator electrical machines with concentrated windings. The increase in efficiency, torque and power density is however limited: Skin and proximity effect lead to increased losses at high frequencies. Additionally, the production process of the coil leads to a non-ideal geometry and therefore to an elevated resistance of the coil. Furthermore, there is no available state-of-the-art insulation system for the preformed coils which are studied in the present work. Newly developed insulation systems might not meet the same thermal requirements as conventional enameled wire. In this paper, the operating limitations of two electrical machines, one with a classical round wire winding and one with preformed coils, are compared. The results are validated using test bench data.**

**Keywords— electrical machines, preformed coils, insulation system, thermal modelling**

## I. Introduction

To further increase the torque density of high torque low speed electrical machines, high slot fill factors are required. Compared to conventional round wire windings, the copper fill factor can be further increased by applying preformed coils with a rectangular cross section. Such coils can be produced by using a forming process, which is introduced in [1]. During this production process, a semi-finished coil is compressed to form the final product. In Fig. 1, the cross sections of the semi-finished and the final coil are displayed, along with a photo of the finished and coated coil.

In the following, two electrical machines are compared to each other. One is equipped with classical round wires, the other one with the newly developed coils. The iron core of both machines is identical. Compared to a classical round wire winding, the innovative coil topology will show a different behavior with respect to the following aspects:

- Insulation system,
- Electromagnetic behavior and
- Thermal behavior.

All these aspects have an influence on the operating limitations of the electrical machine. The maximum temperature of the machine is limited by the thermal class of the insulation system. The electromagnetic behavior defines the losses of the machine depending on the working point in the torque-speed map, while the thermal behavior defines the temperature of the machine as a function of the losses.

The primary insulation of conventional round wires is applied in a continuous process which is not suitable for the coil, studied in the scope of this paper. Therefore, an epoxy coating is applied after the finished forming process. As the utilized material is not a conventional insulation material for the windings of electrical machines, accelerated aging tests are conducted to determine the thermal index of the insulation system and to qualify the insulation following *IEC 60034-18-21* [2]. The aging conditions in detail are introduced in [3]. In this paper the final results of the lifetime tests are presented.

The majority of the machine losses are so called copper losses, which originate from the winding resistance, and the iron losses, which occur due to an oscillating magnetic field in the core material. The approach of substituting the machine winding, which is chosen in the present paper, leaves the iron losses unchanged. The increased copper factor of the machine with preformed coils leads to reduced copper losses. However, the cross-sectional area of the preformed coils is significantly larger than for a comparable round wire. From the application of hairpin windings, it is known that large conductor cross sections lead to more pronounced skin and proximity effects at high speeds [4], which diminish the advantage of an increased copper factor. To study this, electromagnetic finite element simulations and test bench trials are performed. The efficiency of both machines is simulated and measured for the entire torque-speed map.

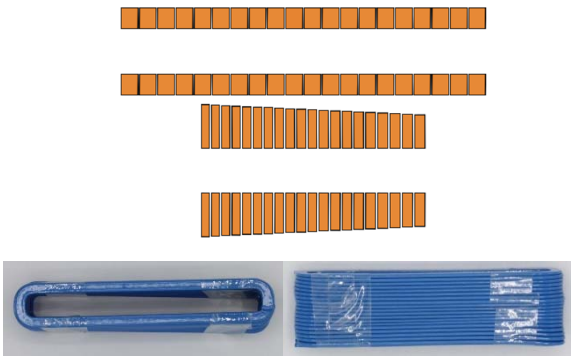

Fig. 1: Cross section of semi-finished coil (top), cross section of the final coil (mid) and photo of the final coil (bottom).

This research and development project is funded by the German Federal Ministry of Education and Research (BMBF) within the Framework Concept "Serienflexible Technologien für elektrische Antriebe von Fahrzeugen 2". The authors are grateful to the BMBF for the financing of this collaboration and are responsible for the contents of this publication. Furthermore, we want to thank our project partners Schaeffler AG, Breuckmann GmbH and the Institute of Metal Forming (IBF) from RWTH Aachen University for the excellent collaboration concerning this project.

978-1-7281-8458-6/20/$31.00 ©2020 IEEE

Authorized licensed use limited to: Universitaetsbibliothek der RWTH Aachen. Downloaded on October 19,2021 at 11:29:05 UTC from IEEE Xplore. Restrictions apply.

As high temperature causes accelerated aging of the insulation system [5, 6], the thermal behavior of the innovative winding is studied. To estimate the operational limitations of the machine with conventional winding and of the machine with preformed coils for various load scenarios, thermal models are set up for both cases. Utilizing testbench data, a lumped parameter thermal model such as presented in [7] or [8] is parametrized.

## II. Characterization of the Insulation System

In Fig. 2 the cross section of a slot is displayed. The primary insulation is directly applied on the surface of the copper conductors. Surface insulation material ensures an advanced insulation between the winding and the stator lamination or between conductors of different phases respectively. To enhance mechanical stability and voltage level, and to protect the winding from ambient influences, impregnation is inserted into the slot.

In this paper, special attention is drawn to the primary insulation, as a conventional enameling process is not suitable for the studied coil geometry. To coat the preformed coils, a two-component epoxy system is applied. As this material is not a conventional insulation material for the winding of electrical machines, accelerated tests are performed to qualify the insulation material. For this purpose, motorettes with semi-finished coils are setup as shown in Fig. 3. The specimens are subjected to an accelerated aging cycle which is displayed in Fig. 4. Following *IEC 60034-18-21* [2], three groups of motorettes are formed and exposed to different temperatures (Table I). For statistical reliable results, it is suggested to perform accelerated aging with at least ten motorettes per group. However, due to issues in the production process of the motorettes, only six respectively five motorettes are tested per load point in this paper.

The insulation's resistance, capacitance, loss factor and partial discharge inception voltage (PDIV) are monitored to detect the end of life of the motorettes [3]. Defective specimens are marked as defect but not sorted out, and are again tested in the following cycles. In the following, the monitored parameters are presented.

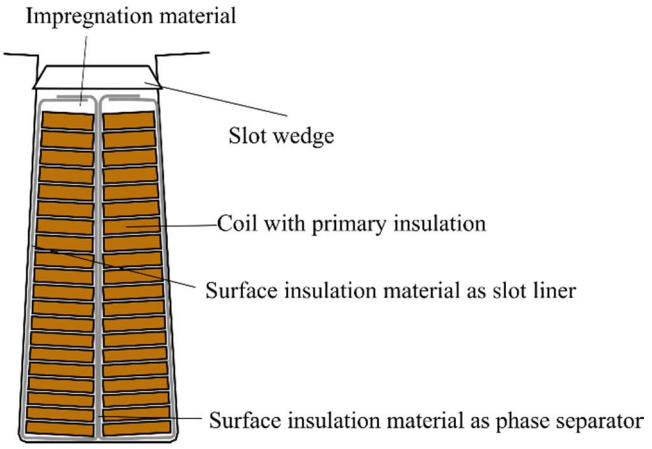


Fig. 2: Cross section of a slot including the coil and the insulation system.

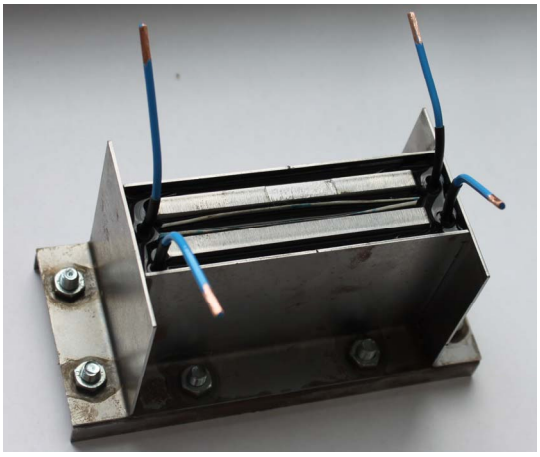

Fig. 3: Motorette with semi finish.

Table I: Dimensions of formed conductors.

| Motorette group | Temperature in °C | Time in d | Estimated number of cycles | Number of motorettes |
|---|---|---|---|---|
| A | 150 | 14 | 10 | 6 |
| B | 170 | 4 | 10 | 6 |
| C | 180 | 2 | 10 | 5 |

### A. Capacitance and Loss Factor

In Fig. 5, the capacitance and the loss factors of the motorettes from group C are displayed. Significant outliers are removed. The error-bars depict the mean of the remaining values and a range of the standard deviation $\sigma$ around the mean value. It can be seen that the loss factor and capacitance increase in the first three cycles. In section II D it can be seen that for motorette group C the first specimen fails after eight cycles.

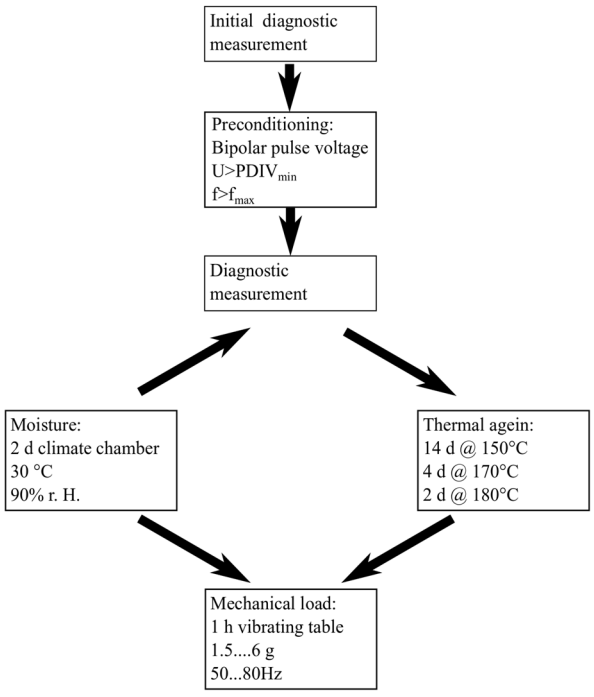


Fig. 4: Test cycle for accelerated thermal aging of the insulation system [3].

Authorized licensed use limited to: Universitaetsbibliothek der RWTH Aachen. Downloaded on October 19,2021 at 11:29:05 UTC from IEEE Xplore. Restrictions apply.

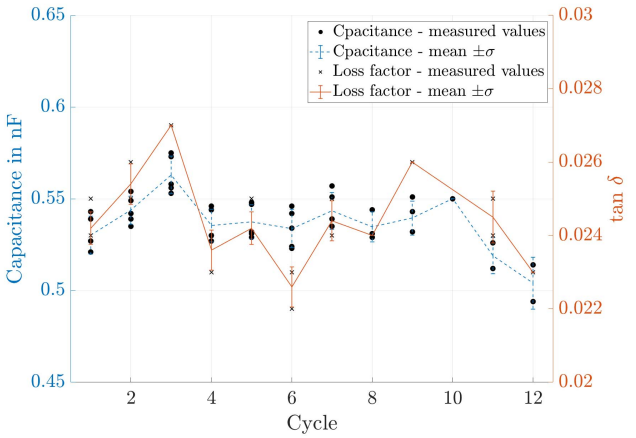


Fig. 5: Capacitance and loss factor between the two coils for motorettes of group C.

From this point, the number of measurements that lead to implausible results is increased significantly, such that for several measuring points only data from one or two specimens is available. After ten cycles the measured capacitance starts to decrease. The increase of the capacitances can be accounted to an ongoing curing process of the impregnation material [9]. The decrease of the capacitance in the last aging cycles is caused by material loss and cracks inside the impregnation material.

### *B. Insulation Resistance*

The insulation resistance is measured between the two coils of the motorette and between the coil and supporting metal sheet structure, respectively at a direct voltage of 1000 V. The measuring results are displayed in Fig. 6. For the unaged motorettes, a resistance of approximately 1 GΩ between the two coils and 3.5 GΩ between each coil and the metal sheet construction is measured. This is far more than needed for proper operation of the machine. A decrease of the insulation resistance can indicate modifications inside the insulation system without affecting the functionality of the winding. However, if the insulation resistance is decreased below a certain threshold, the winding is considered as defect. The threshold is set to 5 MΩ in this study. To calculate the mean values and standard deviations, which are depicted in Fig. 6, data from specimens with a resistance of less than 5 MΩ are not considered. The variance of the resistance between phase 2 and ground increases significantly after eight cycles. Also, it can be seen that the insulation resistance between phase 2 and ground seemingly recovers between the measurements after cycle 8 and cycle 9. Such effects can occur due to a conductor displacement because of vibrations, the specimens are subjected to. However, the winding must still be considered defect. Such an apparent annealing can prevent the proper detection of defective motorettes. Therefore, it is suggested to monitor more than just one winding parameter in cyclic aging tests.

### *C. PDIV Measurement*

As the insulation of low voltage machines is rapidly destroyed when subjected to partial discharge (PD), it is considered a failure of the insulation system if the partial discharge inception voltage (PDIV) is below a certain threshold. This threshold can be achieved by applying *IEC 60034-18-41* [10] and depends on the intermediate circuit voltage as well as the operating conditions of the machine. For the considered insulation system, a minimum PDIV of

- $U_{\mathrm{pkpk,min,ph-ph}}$=1180 V and
- $U_{\mathrm{pkpk,min,ph-gd}}$=826 V

is determined for the phase-to-phase and phase-to-ground-voltage respectively. How to obtain these values is discussed in detail in [3].

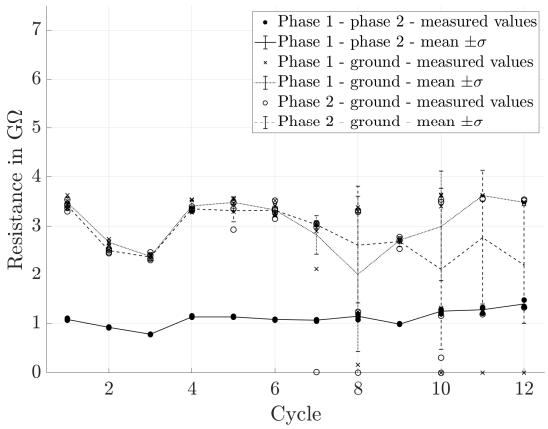


Fig. 6: Insulation resistance for the motorettes of group C.

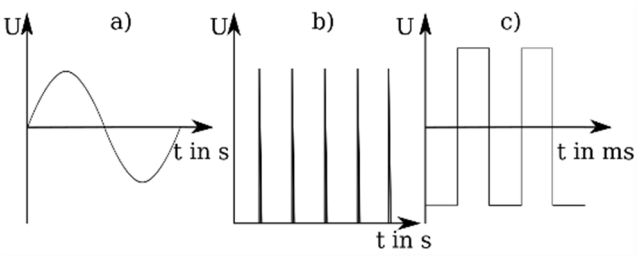


Fig. 7: Different voltage waveforms for PDIV measurement [11].

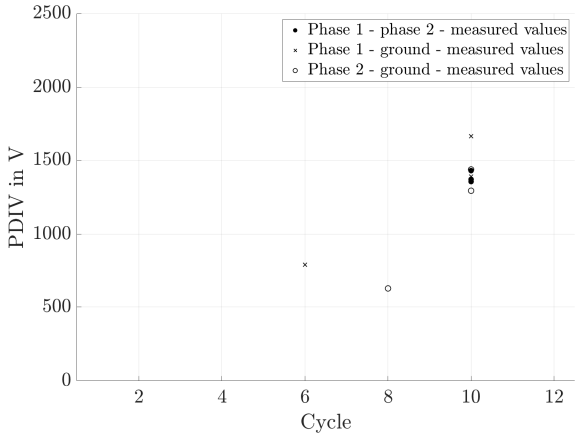


Fig. 8: Measured PDIVs for motorette group C for a sinusoidal voltage.

To measure the PDIV, the motorette is subjected to a voltage, which is ramped up until first PDs occur. At extremely high voltages there is a risk of an electric breakdown, which can cause an irreversible failure of the winding. Therefore, the maximum test voltage is limited to a peak-to-peak-voltage of

Authorized licensed use limited to: Universitaetsbibliothek der RWTH Aachen. Downloaded on October 19,2021 at 11:29:05 UTC from IEEE Xplore. Restrictions apply.

2000 V for phase-to-phase-voltages and 1600 V for phase-to-ground-voltages. The PDIVs are measured for three different voltages waveforms, which are displayed in Fig. 7:

a) Sinusoidal,
b) Unipolar pulse and
c) Bipolar pulse.

For a sinusoidal voltage of 50 Hz, PD only occurs occasionally (Fig. 8). For unipolar pulses, no partial discharge is detected throughout the entire measurement series.

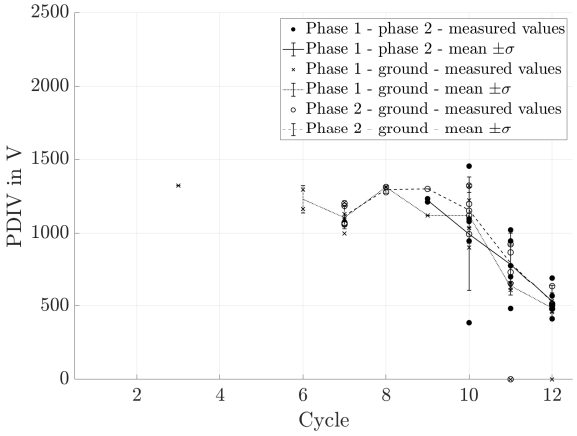


Fig. 9: Measured PDIVs for motorette group C for bipolar voltage pulses.

The measured PDIVs for a bipolar voltage pulse for motorette group C are displayed in Fig. 9. In the first cycles, no PD is measured because the PDIV is above the previously defined maximum of the applied voltage. After six cycles the measured PDIVs decrease gradually.

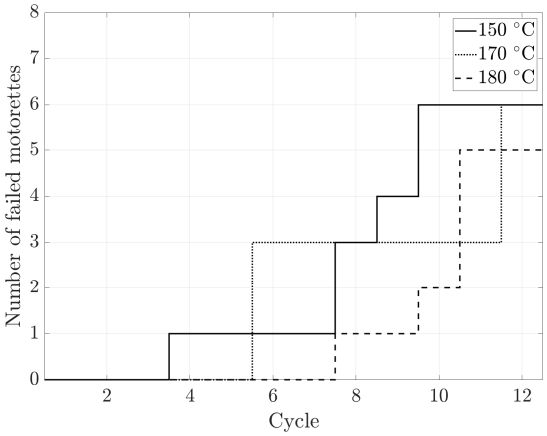


Fig. 10: Number of failed motorettes depending on the number of load cycles.

### *D. Lifetime Estimation*

In Fig. 10, the number of motorettes, that fail to meet the threshold of resistance and PDIV measurement, are displayed depending on the number of cycles. As the motorette can fail at any point of time within the cycle, but is tested only after a cycle is finished, the number of effectively absolved cycles $N_{\mathrm{eff}}$ is calculated by subtracting 0.5 from the number of cycles where the failure is detected $N_{\mathrm{detection}}$:

$$N_{\mathrm{eff}} = N_{\mathrm{detection}} - 0.5. \qquad (1)$$

If the end of life of an exemplary coil is detected after ten cycles, the effective number of absolved cycles is 9.5.
One possibility to describe the temperature dependence of the lifetime is the *Dakin* model:

$$L = A \cdot \exp\left(\frac{B}{T}\right). \qquad (2)$$

The lifetime $L$ decreases as the absolute temperature $T$ is increased. $A$ and $B$ are material dependent parameters, which are determined by evaluating the results of the accelerated aging tests.

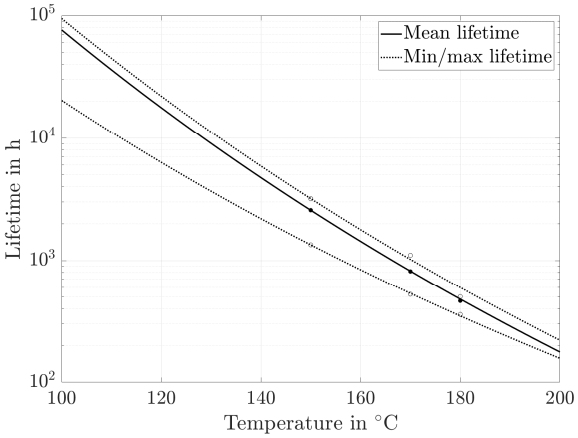


Fig. 11: Estimated lifetime of the motorettes in dependence of the temperature.

In Fig. 11, the *Dakin* model is applied for the mean lifetime as well as for the minimum and maximum lifetime that is achieved for each operating point. The mean lifetime at a temperature of 120 °C is 17,760 h, which is less than the expected lifetime of standard insulation materials at their temperature index (20,000 h), but more than the service life of the average passenger car (6,000… 8,000 h) [12].

## III. Electromagnetic Machine Analysis

An electrical machine with classical round wires and a machine with the innovative coil geometry is studied by means of finite element analysis and test bench measurements. In the following, the machine with a conventional round wire winding is described by the term reference machine, while the machine which is equipped with the innovative coils is called prototype.

TABLE III: Data of the Studied Electrical Machine.

| Parameter | Symbol | Value |
|---|---|---|
| Nominal Current | $\boldsymbol{I_N}$ | 135 A |
| Maximum Current | $I_{\mathrm{P}}$ | 260 A |
| Corner Speed | $n_{\mathrm{N}}$ | 750 rpm |
| Maximum Speed | $n_{\mathrm{max}}$ | 1200 rpm |
| Nominal torque | $T_{\mathrm{N}}$ | 517 Nm |
| Maximum torque | $T_{\mathrm{P}}$ | 838 Nm |
| DC-link voltage | $U_{\mathrm{DC}}$ | 300 V |
| Number of pole pairs | $p$ | 20 |

Authorized licensed use limited to: Universitaetsbibliothek der RWTH Aachen. Downloaded on October 19,2021 at 11:29:05 UTC from IEEE Xplore. Restrictions apply.

### A. Machine topology

The introduced coil geometry is only suitable for machines with concentrated windings. Therefore, a permanent magnet excited wheel hub motor with said winding is studied. The basic data of the machine is given in Table II.

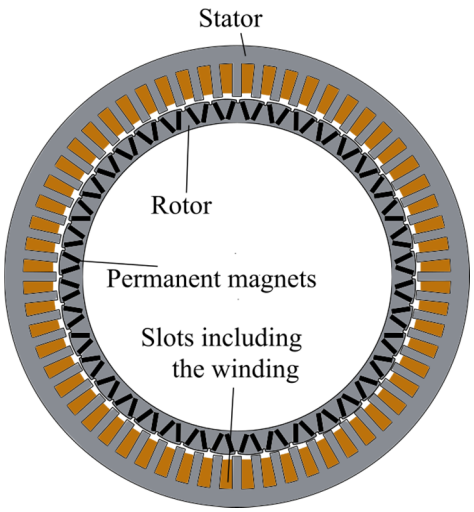


Fig. 12: Scheme of the cross section of the studied machine.

A scheme of the cross section is displayed in Fig. 12. The geometry of the stator iron is identical for both studied machines. After finishing the tests of the reference machine, the rotor is removed and placed inside the prototype. Thus, the influence of deviations from the hard and soft magnetic components of the machine is minimized.

### B. Machine Simulation Methodology

The magnetic field density inside the soft magnetic material is calculated by applying a static 2D finite element simulation.

The torque-speed map is achieved by applying maximum torque per ampere (MTPA) control. The copper losses of the reference machine are calculated according to

$$P_{\mathrm{Cu,Reference}} = \frac{3}{2} \cdot R_{\mathrm{ll}} \cdot I^2 \,, \tag{3}$$

where $I$ is the phase current. The line-to-line-resistance $R_{\mathrm{ll}}$ is measured. For the reference machine, skin and proximity effects are not considered due to the small conductor cross section.

To consider the influence of skin and proximity effect of the prototype, a transient electromagnetic 2D simulation is performed and the AC resistance $R_{\mathrm{ll,AC,sim}}(M,n)$ for the torque-speed map is obtained. The 2D simulation does not consider the end-winding. Therefore, the results of the simulation are adapted by applying a factor $F_{\mathrm{R}}$ which is calculated as a fraction of measured and simulated DC resistance $R_{\mathrm{ll,DC,measured}}$ respectively $R_{\mathrm{ll,DC,simulated}}$:

$$F_{\mathrm{R}} = \frac{R_{\mathrm{ll,DC,measured}}}{R_{\mathrm{ll,DC,simulated}}} \,. \tag{4}$$

The copper losses of the prototype are consequently calculated by applying

$$P_{\mathrm{Cu,Reference}} = \frac{3}{2} F_{\mathrm{R}} \cdot R_{\mathrm{ll,AC,sim}}(M,n) \cdot I^2 \,. \tag{5}$$

The iron losses are calculated according to the formulation presented in [13] and [14], where $B$ is the amplitude of the magnetic field density, $f$ is the electric frequency and $\alpha$, as well as $a_1 \ldots a_5$ are material dependent parameters:

$$P_{\mathrm{Fe}} = a_1 B^{\alpha} f + a_2 B^2 f^2 (1 + a_3 B^{a_4}) + a_5 B^{1.5} f^{1.5} \,. \tag{6}$$

The parameters $\alpha$ and $a_4$ are set to 2 and 4 respectively, while the remaining parameters are fitted to the losses which are obtained from the testbench measurements $P_{\mathrm{Fe,testbench}}$. For this purpose, the calculated copper losses $P_{\mathrm{Cu}}$ are subtracted from the measured total losses $P_{\mathrm{tot}}$:

$$P_{\mathrm{Fe,testbench}} = P_{\mathrm{tot}} - P_{\mathrm{Cu}} \,. \tag{7}$$

Friction losses are not considered.

### C. Test Bench Setup

For the characterization of the machine, a setup such as depicted in Fig. 13 is used. The load machine and the device under test are fed by two different three phase test bench inverters. The machine control is implemented in Matlab Simulink running on a dSpace DS1006 system. Currents and voltages that are fed to the device under test are measured by three LEM current sensors and a voltage transducer respectively. The data acquisition is realized by a Yokogawa WT 3000 power analyzer. The motor is preconditioned with a water ethylene mixture of 50/50 with a flow rate of 7.5 l/min and a controlled temperature of 20 °C. The torque and the speed of the machine are measured by a torque transducer of type HBM T12.

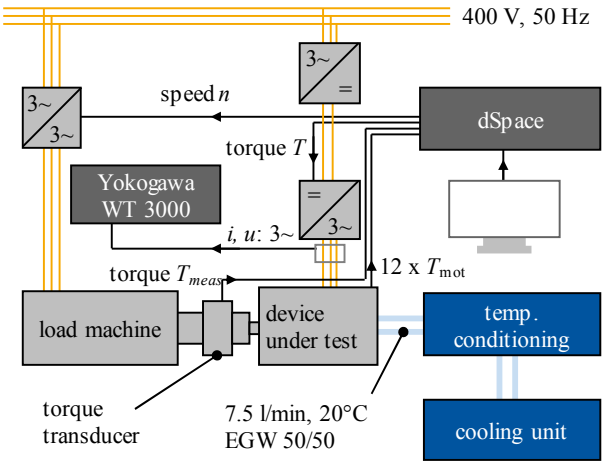


Fig. 13: Schematic overview of machine test-bench setup.

### D. Measurement Preparation

To verify that the excitation of both machines is identical, the no load voltage and the drag torque are measured. For this purpose, the device under test is disconnected from the inverter and accelerated using the load machine, while the terminal voltage and the drag torque are measured. The results

Authorized licensed use limited to: Universitaetsbibliothek der RWTH Aachen. Downloaded on October 19,2021 at 11:29:05 UTC from IEEE Xplore. Restrictions apply.

for the reference machine and the prototype are displayed in Fig. 14. No significant difference between the induced voltages can be spotted (Fig. 14 a)). At high speeds, the drag torque of the prototype is higher than for the reference machine (Fig. 14 b)). Due to the larger cross section of the conductors, additional eddy currents are induced inside the slots which lead to increased losses.

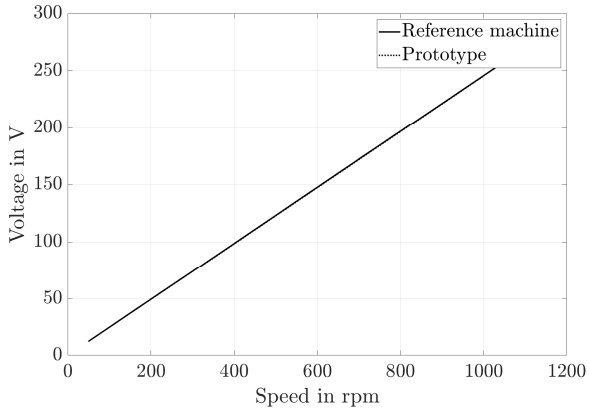


a) Induced voltage of reference machine and prototype.

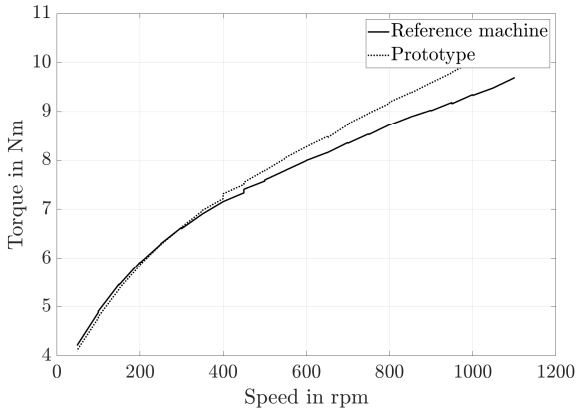


b) Drag torque of reference machine and prototype.

Fig. 14: No load measurements of both machines.

The efficiency of the machines is evaluated at grid points which are placed at steps of 50 Nm respectively 50 rpm. During the measurement, the end winding temperature is monitored. It remains in a range of 25 °C up to 40 °C for all studied operating points.

### *E. Results of the Efficiency Analyis*

The measured and simulated efficiencies of the prototype and the reference machine are displayed in Fig. 15. The measured maximum efficiency of the reference machine (95.14 %) is roughly the same as for the prototype (95.03 %). However, for high torques and low speeds the efficiency of the prototype is significantly higher.

In Fig. 16, the difference between the measured losses are displayed. For positive values the efficiency of the prototype is higher and for negative values the efficiency of the reference machine is higher. For torques close to 0 Nm and high speeds, the measured losses of the prototype are also lower. This effect can be contributed to a deviation in estimating the position of the d- and q-axis for the testbench setup.

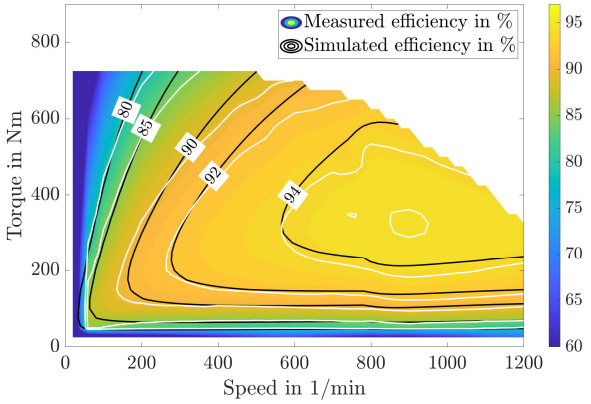


a) Torque-speed-efficiency-map of the reference machine.

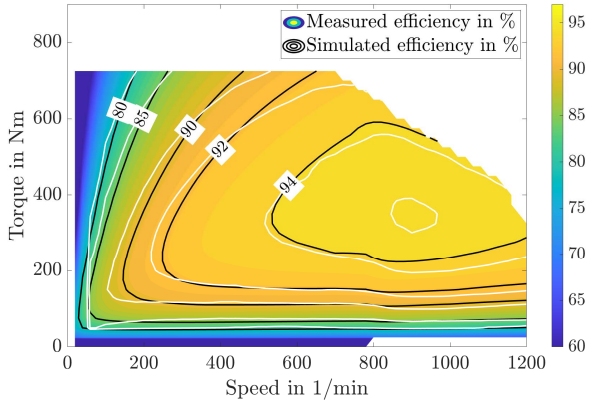


b) Torque-speed-efficiency-map of the prototype.

Fig. 159: Measured and simulated torque-speed-efficiency maps.

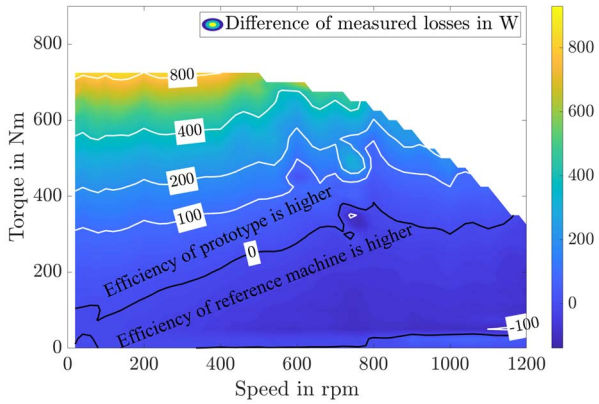


Fig. 16: Difference between measured losses of the reference machine and the prototype.

## IV. Thermal Machine Analysis

For thermal analysis, a lumped parameter model with 67 nodes is created and parametrized based on the machine's geometry and measurement data.

### *A. Parametrization of Thermal Model*

The two different motors are equipped with twelve thermocouples type J per motor. The sensors are numbered and arranged in four different groups as shown in Fig. 17. Two sensors for each phase are placed in the end-winding region (A: Ewdg). Two different sensors are placed in a groove of the

Authorized licensed use limited to: Universitaetsbibliothek der RWTH Aachen. Downloaded on October 19,2021 at 11:29:05 UTC from IEEE Xplore. Restrictions apply.

stator teeth measuring the average temperature between the stator lamination and the housing (B: Lam – Hous). Two different sensors are placed in the slot center of the machine (C: Slot Center). The last two sensors are placed in the potting region between the end winding and the housing (D: Potting).

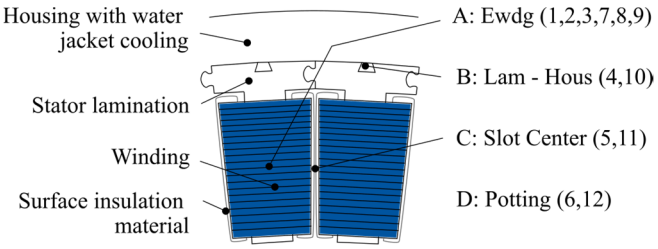


Fig. 17: Placement of thermo elements.

Four different operational points (OPs) for thermal transient operations are studied. The machine torque and speed as well as the measurement time in transient operation are depicted in Table IIII. OP 1 is selected in the base speed region with high torque and high copper losses. OP 2 and OP 3 are in the field weakening region with no load and medium load respectively. OP 4 represents the maximum load point at maximum speed.

TABLE IIII: OPERATIONAL POINTS FOR TRANSIENT MEASUREMENT.

| Operational point | Torque in Nm | Rotational speed in rpm | Transient measurement time |
|---|---|---|---|
| OP 1 | 650 | 50 | 900 |
| OP 2 | 0 | 800 | 1200 |
| OP 3 | 400 | 800 | 500 |
| OP 4 | 300 | 1200 | 900 |

### *B. Results of the Thermal Parametrization*

Based on the simulation model, the machine losses can be split into three different components:

- Copper losses which occur in the stator winding,
- Iron losses which occur in the stator yoke and teeth and
- Iron losses which occur in the rotor.

These loss components are fed into the thermal model. For the time being, the model is solely parametrized for the reference machine. The six sensors in the end-winding in group A heat up uniformly. A maximum deviation of 5 °C is observed for OP 1. Group B and D show a maximum deviation of 1 °C, the sensors of group C of 6 °C. No outliers of the temperature sensors are observed. Due to the minor deviations between the sensors of each group, the values are averaged and used for further analysis.

In Fig. 18, the transient temperature curves of the parametrized simulation model and the measurement data are compared for an exemplary operation point of $n$ = 50 rpm and $T$ = 650 Nm.

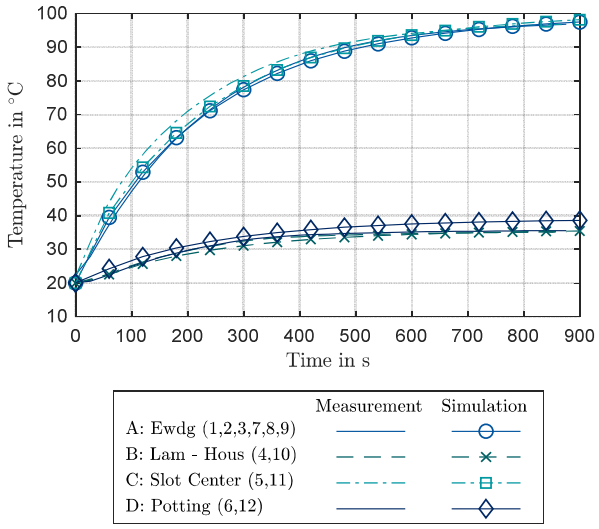


Fig. 18: Transient temperature curve at different locations in the stator at operational point of $n$ = 50 rpm and $T$ = 650 Nm.

## V. OPERATIONAL LIMITATIONS

The simulated losses are applied to the same thermal model for both machines. In Fig. 19, the operational limitation for a continuous operation (S1) are displayed for maximum winding temperatures of 120 °C and 180 °C. A maximum magnet temperature of 120 °C is assumed.

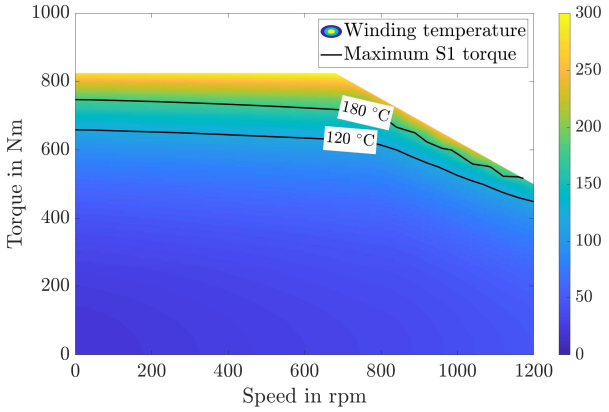


a) Simulated hotspot temperatures for the reference machine.

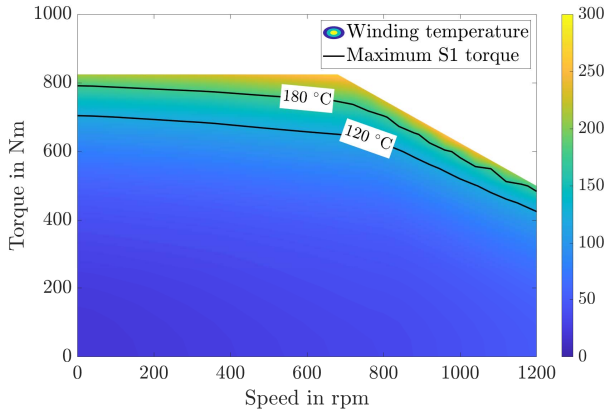


b) Simulated hotspot temperatures for the prototype.

Fig. 19: Simulated hotspot temperatures of the winding and torque limitations for a maximum winding temperature of 120 °C resp. 180 °C and a maximum magnet temperature of 120 °C.

Authorized licensed use limited to: Universitaetsbibliothek der RWTH Aachen. Downloaded on October 19,2021 at 11:29:05 UTC from IEEE Xplore. Restrictions apply.

The limited magnet temperature effects the maximum torque for the insulation class of 180 °C for speeds of $n > 650$ rpm. For a maximum winding temperature of 180 °C, the simulated maximum continuous torque of the prototype is 40 Nm higher than for the reference machine. However, the maximum permissible operational temperature for the protype winding does not exceed 120 °C while state of the art round wire windings can reach end winding temperatures of more than 180 °C. The torque limit of the prototype is therefore decreased by 45 Nm if such a temperature class is assumed for the conventional insulation system.

## VI. Conclusions

A methodology to characterize the operating limitations of a low voltage traction drive is introduced. For this purpose, the thermal limitations of the insulation system are studied along with the electromagnetic and thermal behavior of the machine. The approach to enhance the operating limitations, which is chosen in this machine, is to increase the copper factor by replacing a conventional round wire winding with preformed coils. It is shown that not only the copper filling factor, but also the thermal index of the insulation system must be focused on. For the present example, the introduced winding topology leads to significantly increased efficiency at high torques. However, the low thermal class of the utilized primary insulation materials reduces the maximum torque compared to a motor with a conventional round wire winding. By thermal modeling, it can be shown that the continuous torque can be increased by more than 5 % if the same insulation material is applied for both investigated machines, while the low thermal index of the insulation of the prototype, leads to a decreased torque density compared to a conventional insulation system. Future work focuses on the qualification of alternative insulation materials.

## References


[1] D. Petrell, M. Teller, G. Hirt, S. Börzel and W. Schäfer, "Manufacturing of Conically Shaped Concentrated Windings for Wheel Hub Engines by a Multi-Stage Upsetting Process", *9th International Electric Drives Production Conference (EDPC)*, pp. 1–7, Esslingen, Germany, 2019.

[2] IEC 60034-18-21:2012: "Functional evaluation of insulation systems - Test procedures for wire-wound windings - Thermal evaluation and classification", July 2013.

[3] F. Pauli, M. Schröder and K. Hameyer, "Design and Evaluation Methodology for Insulation Systems of Low Voltage Drives with Preformed Coils", *9th International Electric Drives Production Conference (EDPC)*, pp. 1–7, Esslingen, Germany, 2019.

[4] C. Du-Bar and O. Wallmark, "Eddy Current Losses in a Hairpin Winding for an Automotive Application", *XIII International Conference on Electrical Machines (ICEM)*, pp. 710–716, Alexandroupoli, 2018.

[5] P. Giangrande, V. Madonna, S. Nuzzo and M. Galea, "Moving Toward a Reliability-Oriented Design Approach of Low-Voltage Electrical Machines by Including Insulation Thermal Aging Considerations", *IEEE Transactions on Transportation Electrification*, vol. 6, no. 1, pp. 16–27, March 2020.

[6] T. W. Dakin, "Electrical insulation deterioration treated as a chemical rate phenomenon", Transactions of the American Institute of Electrical Engineers, vol. 67, no. 1, pp. 113–122, 1948.

[7] B. Groschup, M. Komissarov, S. Stevic and K. Hameyer, "Operation Enhancement of Permanent Magnet Excited Motors with Advanced Rotor Cooling System", *IEEE Transportation Electrification Conference and Expo (ITEC)*, pp. 1–6, Detroit, MI, USA, 2019.

[8] A. Boglietti, A. Cavagnino, D. Staton, M. Shanel, M. Mueller and C. Mejuto, "Evolution and Modern Approaches for Thermal Analysis of Electrical Machines", *IEEE Transactions on Industrial Electronics*, vol. 56, no. 3, pp. 871–882, March 2009.

[9] M. Farahani, H. Borsi, E. Gockenbach and M. Kaufhold, "Partial discharge and dissipation factor behavior of model insulating systems for high voltage rotating machines under different stresses", *IEEE Electrical Insulation Magazine*, vol. 21, no. 5, pp. 5–19, Sept.-Oct. 2005.

[10] IEC 60034-18-41 ed. I, Rotating electrical machines – Part 18-41: Partial discharge free electrical insulation systems (Type I) used in rotating electrical machines fed from voltage converters – Qualification and quality control tests, 2014.

[11] F. Pauli, A. Ruf and K. Hameyer, "Low voltage winding insulation systems under the influence of high du/dt slew rate inverter voltage", *Archives of electrical engineering,* vol. 69, pp. 187–202, Warsaw, 2020.

[12] R. Rothe and K. Hameyer, "Life expectancy calculation for electric vehicle traction motors regarding dynamic temperature and driving cycles", *IEEE International Electric Machines & Drives Conference (IEMDC)*, pp. 1306–1309, Niagara Falls, ON, 2011.

[13] D. Schmidt, M. van der Giet and K. Hameyer, "Improved iron-loss prediction by a modified loss-equation using a reduced parameter identification range", 20th international conference on Soft magnetic materials (SMM), Kos Island, September 2011.

[14] D. Eggers, S. Steentjes and K. Hameyer, "Advanced Iron-Loss Estimation for Nonlinear Material Behavior", *IEEE Transactions on Magnetics*, vol. 48, no. 11, pp. 3021–3024, Nov. 2012.


Authorized licensed use limited to: Universitaetsbibliothek der RWTH Aachen. Downloaded on October 19,2021 at 11:29:05 UTC from IEEE Xplore. Restrictions apply.